

## Impact of Radiation on the LHCb VELO Sensors

---

**A.D. Webber**<sup>\*†</sup>

*The University of Manchester, United Kingdom*

*E-mail: [adam.webber@hep.manchester.ac.uk](mailto:adam.webber@hep.manchester.ac.uk)*

The Vertex Locator (VELO) is a silicon microstrip detector, designed to reconstruct charged particle trajectories and vertices produced at the LHCb interaction region. During 2010 and 2011 the VELO sensors were exposed to fluences of up to around  $45 \times 10^{12}$  1 MeV neutron equivalent ( $1 \text{ MeV n}_{\text{eq}}$ ). The silicon effective bandgap has been determined in VELO sensors using current versus temperature data, with an average value of  $E_g = 1.16 \pm 0.03 \pm 0.04 \text{ eV}$  obtained after sensor irradiation. The first observation of  $n^+$ -on- $n$  sensor type inversion at the LHC is reported, occurring at a fluence of around  $(10 - 15) \times 10^{12}$  of  $1 \text{ MeV n}_{\text{eq}}$ . The only  $n^+$ -on- $p$  sensors in use at the LHC have also been studied, for which a decrease in the Effective Depletion Voltage (EDV) of  $\sim 25 \text{ V}$  is observed, following an initial fluence of approximately  $3 \times 10^{12}$   $1 \text{ MeV n}_{\text{eq}}$ . After this, the EDV in  $n^+$ -on- $p$  type sensors is found to increase at a comparable rate to type inverted  $n^+$ -on- $n$  type sensors. A reduction in the charge collection efficiency is observed, due to an effect involving the second metal layer readout lines.

*The 21st International Workshop on Vertex Detectors  
16-21 September 2012  
Jeju, Korea*

---

<sup>\*</sup>Speaker.

<sup>†</sup>On behalf of the LHCb collaboration.

## 1. Introduction

The VERtEX LOcator (VELO) is a silicon strip detector located around the proton-proton interaction region at the LHCb experiment [1]. The closest active silicon sensor regions are located only 8.2mm from the beam axis, providing the high precision vertex reconstruction required for heavy flavour physics. In this environment the sensors experience high particle fluences, therefore careful monitoring of sensor radiation damage is required.

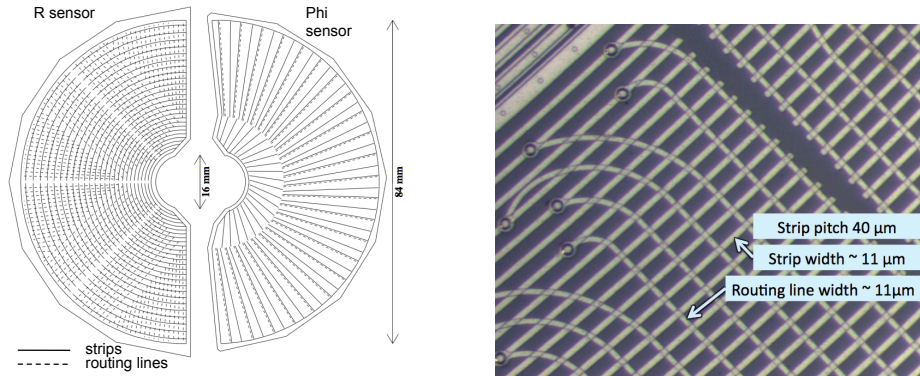


**Figure 1:** (left) A schematic representation of an R-type and a  $\phi$ -type sensor. The signal routing lines are orientated perpendicularly to the R-type strips and parallel to the  $\phi$ -type strips. (right) A photograph of a section of an R-type sensor. Each strip (running from bottom-left to the top-right) is connected to a routing line (running from top-left to the bottom-right).

The VELO comprises two halves, retractable by 29 mm in the horizontal plane. During proton injection and energy ramping of the LHC beams, the VELO halves are retracted to avoid damage to the silicon sensors. When the beams are stable the halves are closed around the beam axis. Each half contains 42 half-disc shaped,  $300\mu\text{m}$  thick silicon sensors, which have been oxygenated (with concentrations greater than  $10^{17}\text{cm}^{-3}$ ) in order to improve their radiation tolerance. Half of the sensors have strips orientated in an approximately radial direction ( $\phi$ -type) and the other half in a circular direction (R-type), as shown in Fig. 1 (left). R-type and  $\phi$ -type sensors are paired in modules, in which a sensor of each type is glued to a common support in a back-to-back configuration. The majority of the sensors are  $n^+$ -on- $n$ , comprising a  $n$ -type implant in a  $n$ -type bulk with a backplane  $p^+$ -type implant. However, two of the sensors use a  $n^+$ -on- $p$  configuration, intended to be a test of one of the leading LHC silicon upgrade candidates in an operational environment.

Each silicon strip has a metal track running along the length of the  $n^+$  implant, which are collectively referred to as the *first metal layer*. Signal readout of the strips is not trivial, as the R-type strips and inner  $\phi$ -type strips do not extend to the outer region of the sensors. To readout signal, each metal track is connected to a *second metal layer* routing line which extends to the electronics at the sensor edge, as shown in Fig. 1 (right). Apart from at the contact points between the strips and routing lines, the first and second metal layers are insulated from one another by  $3.8 \pm 0.3\mu\text{m}$  of  $\text{SiO}_2$ .

## 2. Sensor currents

The leakage current in a silicon sensor is a linear function of fluence for a wide range of silicon substrates [2]. This provides a simple method for relating sensor currents to the particle fluence that a sensor has been exposed to. With a good understanding of sensor annealing conditions, changes in current can be related to the particle fluence incident on the sensor. Using the NIEL scaling hypothesis [3], GEANT4 [4] simulated data have been combined with the recorded temperature history of the VELO sensors to predict the change in sensor current as a function of luminosity [5]. The predictions are compared to measurements from each sensor following  $1.20 \text{ fb}^{-1}$  of delivered luminosity in Fig. 2, with good agreement found. The mean predicted current obtained with this

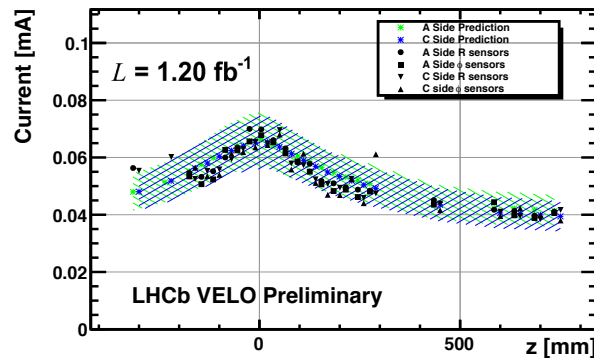


**Figure 2:** The leakage current against sensor  $z$ -coordinate after  $1.20 \text{ fb}^{-1}$  of integrated luminosity, normalised to  $0^\circ\text{C}$ . The data is in agreement with predictions, represented by the dashed region. The two VELO halves are referred to as the A and C sides of the VELO.

method agrees well with sensor measurements, as shown in Fig. 3, in which each sensor current is shown as a function of time. The spread of the values is mostly due to the varying particle fluence experienced by sensors positioned at different distances from the interaction region.

In VELO sensors prior to irradiation, the majority of sensor currents are small and assumed to consist of a mixture of bulk and surface currents. The bulk currents vary exponentially with

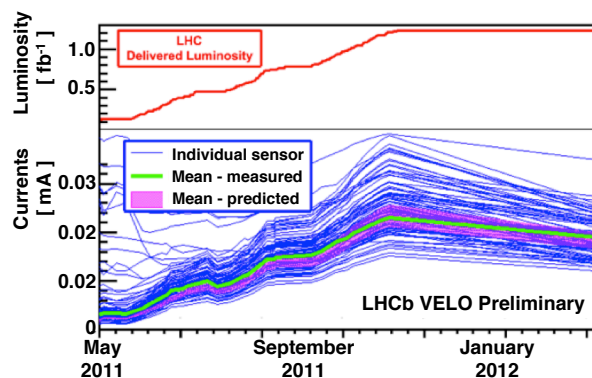


**Figure 3:** (bottom) The measured current in each VELO sensor at 150 V and at a temperature of approximately  $-7^\circ\text{C}$  and (top) the delivered luminosity, each as a function of time. The mean measured current agrees well with the simulated prediction (excluding the surface current dominated sensors).

temperature and have a precisely predicted relationship with fluence, whereas surface currents arise due to imperfections related to sensor production and handling. In the VELO sensors, surface currents are predominantly characterised by an Ohmic increase in current with bias voltage [6]. The relative contribution of bulk and surface current has been identified by measuring the current as a function of temperature (IT scan), as demonstrated by Fig. 4 and described in detail in Ref. [5]. In the majority of sensors the Ohmic surface current is seen to anneal with fluence.

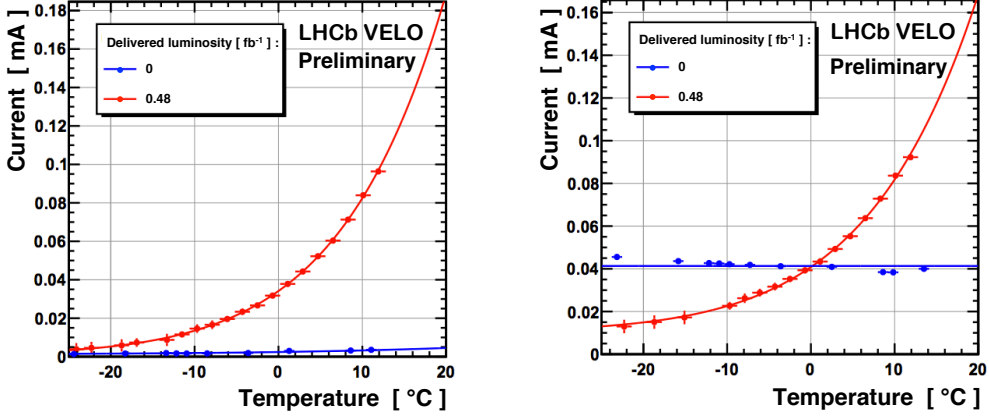


**Figure 4:** The current versus temperature for two VELO sensors, each operated at 150 V. Prior to irradiation there is a small exponential component for the sensor shown on the left, while that shown on the right is dominated by the non-temperature dependent surface current. After irradiation a dominant exponential component is seen for both sensors and the surface current has reduced significantly.

In the temperature range of interest (i.e. that of Fig. 4) the bulk current is expected to scale according to  $I \propto T^2 \exp(-E_g/2kT)$ , where  $T$  is the temperature in Kelvin,  $k$  is the Boltzmann constant and  $E_g$  is a constant related to the bandgap energy that has been measured using IT scan data collected in the VELO. A summary of the results obtained from several IT scans is presented in Table 1. The weighted mean of the various measured values is  $E_g = 1.16 \pm 0.03 \pm 0.04$  eV, which is statistically compatible with the literature value of 1.21 eV [7]. Recent studies [7] have shown that  $E_g$  may be measured systematically high due to sensor self heating, or may depend on the sensor bias voltage. However, the VELO sensors used for these measurements were kept cool (approximately  $-7^\circ\text{C}$ ) and sufficiently biased (150 V) such that these effects should not significantly influence the result, as supported by the consistency of the cross-check measurement made at 100 V.

Delivered luminosity [fb <sup>-1</sup> ]	Bias voltage [V]	$E_g$ [eV]
0.48	100	$1.17 \pm 0.07 \pm 0.04$
0.48	150	$1.18 \pm 0.05 \pm 0.04$
0.82	150	$1.14 \pm 0.06 \pm 0.04$
1.20	150	$1.15 \pm 0.04 \pm 0.04$

**Table 1:** The effective band gap,  $E_g$ , measured using data from four different IT scans after various amounts of delivered luminosity. The first uncertainty is statistical and the second is systematic, which is dominated by the accuracy of sensor temperature determination and the choice of fitting range [5].

### 3. Depletion voltage studies

The depletion voltage of a silicon sensor is defined as the reverse bias voltage required to fully deplete the sensor-bulk of free charge carriers. The effective doping of the  $n$ -bulk changes over time due to radiation-induced defects. This causes the depletion voltages of  $n^+$ -on- $n$  sensors to decrease with fluence, until the  $n$ -type bulk inverts and becomes  $p$ -type. Following this the depletion voltage is expected to increase with irradiation. There are expected to be competing mechanisms for oxygenated  $n^+$ -on- $p$  type sensors, with acceptor introduction partially compensated by initial oxygen induced acceptor removal [8, 9].

Prior to installation, the VELO sensor depletion voltages were determined by measuring the sensor capacitance (C) as a function of bias voltage (V). After installation, an alternative approach has been used to measure an analogous property referred to as the Effective Depletion Voltage (EDV), obtained by measuring the Charge Collection Efficiency (CCE) of a sensor as a function of bias voltage. Special data has been collected for which every fifth module (the *test* sensors) is operated at a voltage ranging between 0 and 150 V. The remaining modules are maintained at the nominal 150 V bias. The test sensors are removed from the track reconstruction algorithms. Tracks are extrapolated to coordinates on the test sensors and the set of five nearest strips are searched for deposited charge (the extrapolation uncertainty is small compared to the strip pitch). At each bias voltage the Most Probable Value (MPV) of the charge distribution is determined. The EDV is defined as the voltage at which the MPV is equal to 80% of its plateau value, as demonstrated by Fig. 5. The 80% threshold was chosen to give closest agreement with the pre-irradiation CV measurements, with differences between the two methods below 10 V for all sensors.

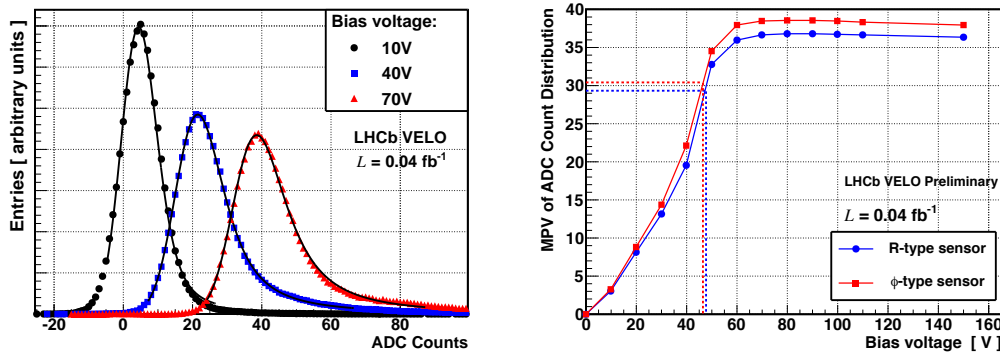


**Figure 5:** (left) The pedestal subtracted charge count (ADC) distribution and fit result for an R-type sensor at three example bias voltages. The MPV is the ADC value that the peak is centred on. (right) The MPV of the ADC distribution versus bias voltage. The dashed lines show the 80% MPVs and corresponding EDVs.

Five dedicated CCE scans were taken between April 2010 and October 2011, corresponding to data collected after 0, 0.04, 0.43, 0.80 and  $1.22 \text{ fb}^{-1}$  of delivered luminosity. Because the incident particle fluence decreases from low to high sensor radius, each sensor is divided into 5 radial regions, such that the fluence (predicted by simulation) does not change by more than a factor of two across a region. The change in EDV with irradiation for a particular  $n^+$ -on- $n$  type sensor is shown in Fig. 6 (left). The EDV is found to initially decrease with fluence across all radial regions, with the largest decrease observed in the inner radial regions which are exposed to the greatest

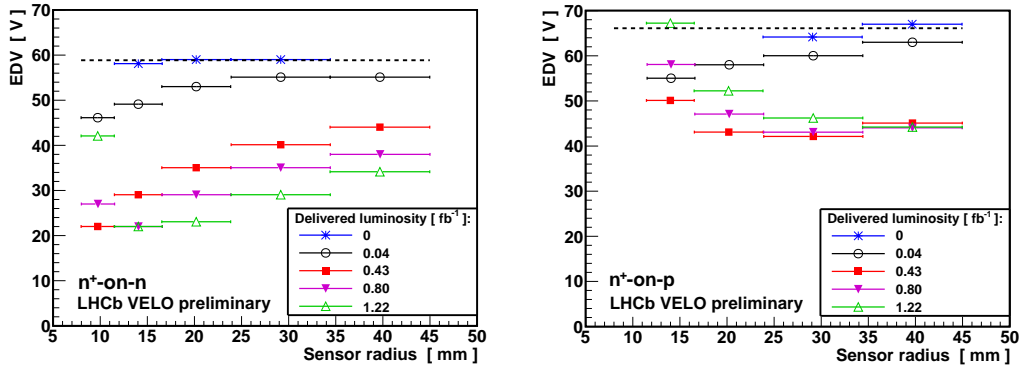


**Figure 6:** The EDV against sensor radius for (left) an  $n^+$ -on- $n$  type sensor and (right) an  $n^+$ -on- $p$  type-sensor. The dashed lines show the mean EDV across all radius regions before irradiation (where some fluence bins do not have EDVs due to low CCE scan statistics). The EDV increase in the innermost  $n^+$ -on- $n$  region for the latter scans indicates that this region has type inverted.

fluence. The  $n^+$ -on- $p$  type sensors exhibit a decrease in EDV with initial fluence, as shown in Fig. 6 (right). This initial EDV decrease is understood to be caused by oxygen induced removal of boron interstitial acceptor sites, an effect that has been previously reported in the literature [8, 9].

The EDV trend of all sensors is shown as a function of fluence in Fig. 7. The Hamburg model predicts that the depletion voltage of  $n^+$ -on- $n$  type sensors will decrease with initial fluence to a value of approximately 0 V. However, the minimum EDV that is measured in any VELO sensor is  $\sim 18$  V, suggesting that near to type inversion the EDV does not accurately describe the sensor depletion voltage. The minimal EDV is dictated by the smallest potential difference required to collect charge from the silicon strips, which in turn depends on the shaping time of the electronics. It is assumed that the sensors type invert at a fluence near to the minimum EDV. For  $n^+$ -on- $n$  type sensors this occurs at approximately the same fluence of  $(10 - 15) \times 10^{12}$   $1 \text{ MeV } n_{\text{eq}}$ , irrespective

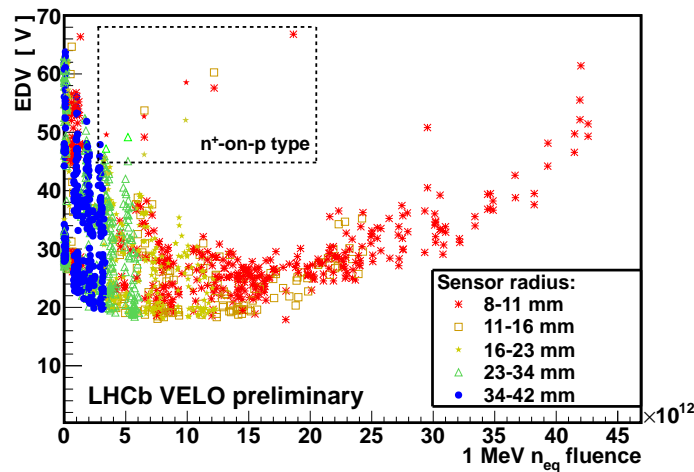


**Figure 7:** The EDV against fluence for each sensor radius region. Data from all CCE scans is displayed. The fluence in each sensor region has been predicted using simulated data with a method that has been validated in studies of sensor currents (see Sect. 2).

of the EDV of the sensor prior to irradiation. The behaviour after inversion is also consistent with being independent of the initial EDV, with an approximately linear increase in EDV with additional fluence. The entries within the dashed box in Fig. 7 correspond to data from the  $n^+$ -on- $p$  sensors. The EDV initially decreased for fluences up to approximately  $3 \times 10^{12}$   $1 \text{ MeV n}_{\text{eq}}$ . After this the EDV increased with fluence at a comparable rate to the type inverted  $n^+$ -on- $n$  sensors.

The Hamburg model can be used to predict sensor depletion voltages as a function of fluence. It has three components related to stable damage, short term annealing and reverse annealing. The VELO sensor temperature history and LHCb luminosity measurements have been used to predict the depletion voltage as a function of fluence, as shown in Fig. 8. Three sets of sensor measurements are compared, each from sensors with different initial EDVs. As discussed previously, significant differences are seen at fluences near to sensor type inversion. Good agreement is found at low fluences and for higher fluences after type inversion.

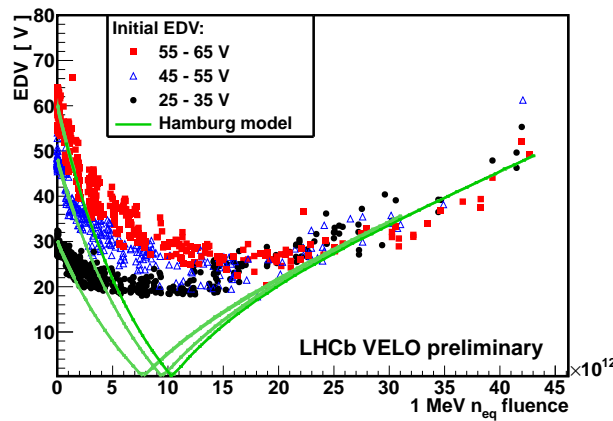


**Figure 8:** The EDV against fluence is compared to Hamburg model predicted depletion voltages.

A second method has been developed to monitor radiation damage in VELO sensors. In undepleted silicon, several sources of input capacitance are identified, one of which is the inter-strip impedance. For  $n^+$ -on- $n$  sensors before type inversion, the depletion region grows with increasing voltage from the backplane (the opposite side to the strips). When the sensor is fully depleted the space-charge reaches the strips and the inter-strip resistance increases significantly [10], resulting in a decrease of the sensor noise. For  $n^+$ -on- $n$  type sensors following type inversion, and for  $n^+$ -on- $p$  type sensors, the depletion region grows from the strip side of the silicon. In this situation the strips are immediately isolated at the application of a bias voltage and the relationship between noise and voltage cannot be exploited as effectively to extract information related to the depletion voltage.

The Noise Effective Depletion Voltage (NEDV) is defined as the voltage at which the  $1/\text{noise}$  has increased to 80% of the maximum. When a sensor is near to type inversion the  $1/\text{noise}$  increases significantly between 10V and 20V, with a very gradual rise thereafter. In this situation the NEDV cannot be determined accurately and a value of 20V is assumed. If the  $1/\text{noise}$  does not change significantly between 10V and 150V the sensor is considered type inverted and an NEDV of 10V is assigned. This approach is demonstrated by Fig. 9 (left). As expected, the noise in the  $n^+$ -on- $p$  type sensor shows little dependence on voltage. The evolution of the NEDV is shown for all R-type sensors as a function of fluence in Fig. 9 (right). Good agreement has been found

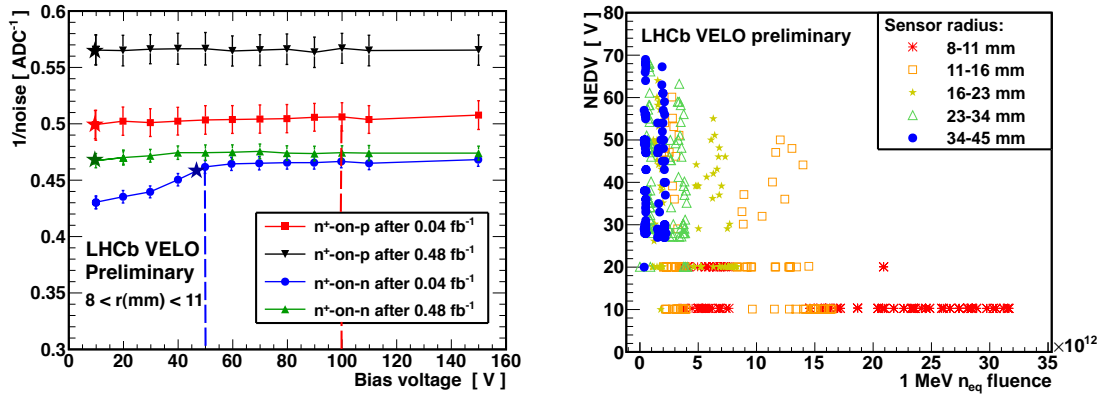


**Figure 9:** (left) The  $1/\text{noise}$  versus voltage for particular  $n^+$ -on- $n$  and  $n^+$ -on- $p$  type sensors at two values of integrated luminosity. The CV scan measured initial depletion voltages and NEDVs are shown by the dashed lines and star symbols respectively. The offset in  $1/\text{noise}$  between sensor types/luminosities is due to a change in the sampling time, which does not influence the determined values of NEDV. (right) The NEDV against fluence for all R-type sensors radius regions.

between the  $n^+$ -on- $n$  type sensors identified as type inverted using this and the CCE method.

#### 4. Charge loss to the second metal layer

The data scans described in Sect. 3 have also been used to measure the Cluster Finding Efficiency (CFE), by looking for the presence of a cluster at the track intercept coordinates with the test sensors. A cluster is defined as one or several adjacent sensor-strips with charge above a particular threshold. Before irradiation the mean CFE in all VELO sensors was greater than 99%. After irradiation the CFE in many sensor regions reduced significantly, with decreases of around 5% observed in the worst effected regions: at large radii and high bias voltages. A large sample of regular LHCb physics data has been used to measure the CFE in small sensor regions, as shown in Fig. 10, displayed beside a schematic of the second metal layer routing lines. High CFE is measured in regions that are devoid of second metal layer lines, indicating that the routing lines play a role in the CFE loss.

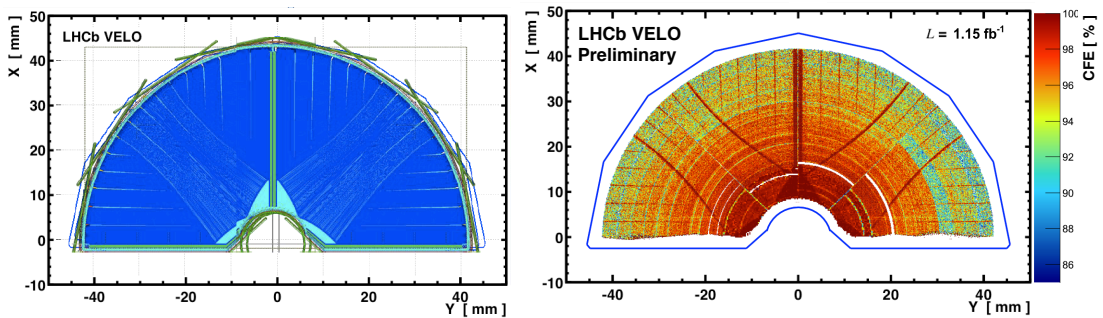


**Figure 10:** (left) The layout of the routing lines on an R-type sensor. The darker regions represent the presence of routing lines, and the lighter regions their absence. (right) The CFE map of an R-type sensor after significant irradiation (at 150 V). High CFE regions match the regions without routing lines.

In R-type sensors the routing lines pass above and approximately perpendicular to the outer strip implants. Using precise track extrapolation, the CFE loss is measured as a function of the distance between a track intercept with a sensor, and the nearest strip and routing line. This is shown in Fig. 11 (left). The CFE is reduced most significantly when a track intercept is far from a strip and near to a routing line. Similar effects have been observed in other experiments [11, 12]. In addition to lowering the CFE, charge induced on routing lines may introduce low ADC noise clusters. The cluster ADC distribution has a peak associated to this that has grown with fluence, as shown in Fig. 11 (right). The fraction of noise induced clusters behaves similarly to the CFE, with greater fractions seen for tracks that are incident near to a routing line and far from a strip.

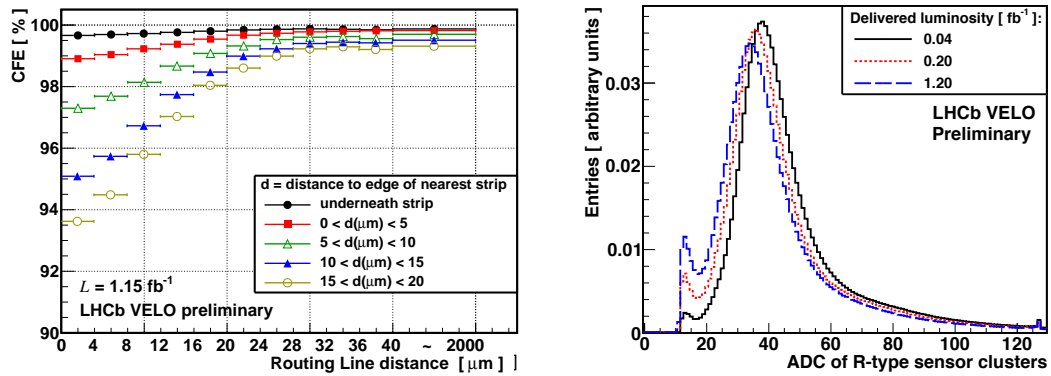


**Figure 11:** (left) The CFE as a function of the distance between the particle intercept and the nearest routing line, for several bins of the distance between the particle intercept and closest strip edge. (right) The ADC spectrum of all clusters seen in R-type sensors at three different integrated luminosities.

The CFE loss mechanism is hypothesised in terms of charge induction on the second metal layer. Prior to irradiation most field lines will terminate at the  $n^+$  implants. However, irradiation may cause modifications to the field line structure, such that not all field lines terminate on the implants. In addition, radiation induced charge trapping defects may delay the drift of charge, resulting in charge sampling before the electrons have reached the implants. In both of these situations a net charge may be induced on nearby electrodes, such as the second metal layer routing lines. In reality, it is likely that the charge loss is due to several competing mechanisms. The CFE decrease is not observed in  $\phi$ -type sensors, as the strip orientation allows for the routing lines from inner strips to be placed directly above the outer strips, thus minimising pick-up.

The MPV of deposited charge is shown as a function of voltage for each sensor type in Fig. 12 (left). At 150 V the MPV of the  $n^+$ -on- $n$  and  $n^+$ -on- $p$  are approximately equal, both before and after irradiation. After irradiation the MPV of the  $n^+$ -on- $n$  sensor peaks at  $\sim 60$  V, following which it decreases with increasing voltage. This decrease in MPV is associated with the second metal layer effect and results in a reduced CFE. It depends on sensor radius similarly to the CFE effect, and is not evident in  $\phi$ -type sensors. The  $n^+$ -on- $p$  sensor does not exhibit the same dependence on voltage, potentially due to the depletion region growing from the strip side of the silicon instead of the backplane. This is supported by the observation that following  $n^+$ -on- $n$  sensors type inversion, the MPVs do not decrease with increasing voltage, as shown in Fig. 12 (right).

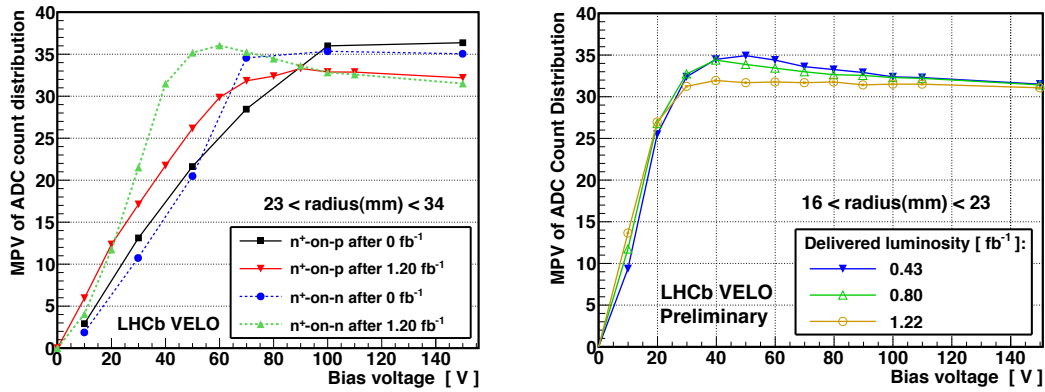


**Figure 12:** (left) A comparison of the MPV versus voltage for each sensor type, before and after irradiation. (right) The MPV versus voltage for an R-type sensor after several amounts of integrated luminosity. The sensor has been identified as having type inverted in the  $1.22 \text{ fb}^{-1}$  scan, for which the plateau voltage dependence is removed.

## 5. Summary

The effects of radiation damage have been observed in all of the LHCb VELO sensors. The silicon effective bandgap has been determined using current versus temperature scan data to be  $E_g = 1.16 \pm 0.03 \pm 0.04 \text{ eV}$ . The noise and Charge Collection Efficiency of sensors have been used to effectively track the evolution of the sensor depletion voltages with fluence. The Effective Depletion Voltages of the two  $n^+$ -on- $p$  sensors decreased with initial fluence. Subsequently they have increased at a comparable rate to the type inverted  $n^+$ -on- $n$  type sensors. A significant decrease in the Cluster Finding Efficiency of R-type sensors has been observed, due to a second metal layer effect. For the  $n^+$ -on- $n$  type sensors before type inversion the charge loss is voltage dependent, whereas for  $n^+$ -on- $p$  and type inverted  $n^+$ -on- $n$  sensors a voltage dependence is not observed.

## References

- [1] The LHCb collaboration, *The LHCb detector at the LHC*, *JINST* **3** S08005 (2008)
- [2] M. Moll, PhD Thesis, *Fachbereich Physik der Universität Hamburg* (1999)
- [3] A. Vasilescu, *ROSE/TN/97-2* (1999)
- [4] S. Agostinelli *et al.*, *Nucl. Instrum. Meth.*, **A506** 250 (2003)
- [5] The LHCb VELO group, LHCb-PUB-2011-021 (2011)
- [6] The LHCb VELO group, LHCb-PUB-2011-020 (2011)
- [7] A. Chilingarov, *Generation current temperature scaling*, PH-EP-Tech-Note-2013-001 (2013)
- [8] F. Lemeilleur *et al.*, *Nuclear Physics B - Proceedings Supplements* **32** 415-424 (1993)
- [9] M. Lozano *et al.*, *IEEE Trans.Nucl.Sci.* **52** 1468-1473 (2005)
- [10] C. Barth, *Nucl. Instrum. Meth.* **A658** 6-10 (2011)
- [11] L. Tommaso, *Test beam results of ATLAS Pixel sensors*, arXiv:hep-ex/0210045v1 (2002)
- [12] T. Rohe *et al.*, *IEEE Trans.Nucl.Sci.* **51** 1150-1157 (2004)